Energy Storage Materials 49 (2022) 278–290

Contents lists available at ScienceDirect

Energy Storage Materials

journal homepage: www.elsevier.com/locate/ensm

A rational design of garnet-type $Li_7La_3Zr_2O_{12}$ with ultrahigh moisture stability

Hongpeng Zheng [a,1], Guoyao Li [a,1], Jiqiong Liu [a], Shaoping Wu [a], Xingmin Zhang [b], Yongmin Wu [c], Hong Zhu [d], Xiao Huang [e,*], Hezhou Liu [a], Huanan Duan [a,*]

[a] State Key Laboratory of Metal Matrix Composites, School of Materials Science and Engineering, Shanghai Jiao Tong University, Shanghai 200240, PR China
[b] Shanghai Synchrotron Radiation Facility, Shanghai Advanced Research Institute, Chinese Academy of Sciences, Shanghai 201204, PR China
[c] State Key Laboratory of Space Power Technology, Shanghai Institute of Space Power-Sources, Shanghai 200245, PR China
[d] University of Michigan-Shanghai Jiao Tong University Joint Institute, Shanghai Jiao Tong University, Shanghai 200240, PR China
[e] SZU-NUS Collaborative Innovation Center for Optoelectronic Science & Technology, International Collaborative Laboratory of 2D Materials for Optoelectronics Science and Technology of Ministry of Education, Institute of Microscale Optoelectronics, Shenzhen University, Shenzhen 518060, PR China

ARTICLE INFO

Keywords:
Lithium garnets
Moisture stability
Solvent-free
Stoichiometric composition
Solid-state lithium batteries

ABSTRACT

Lithium-stuffed garnets, one of the most promising solid electrolytes for all-solid-state lithium batteries (ASSLBs), are typically vulnerable to water or moisture. In this work, $Li_{6.5}La_3Zr_{1.5}Ta_{0.5}O_{12}$ (LLZT) with ionic conductivity of 7.36×10^{-4} S cm^{-1} at room temperature and ultrahigh moisture stability is designed and synthesized by a solvent-free route with no excess lithium source. After storing in ambient atmosphere for four months, the LLZT maintains an ionic conductivity of 6.41×10^{-4} S cm^{-1}. With optimized lithium contents, the LLZT is stored in an atmosphere rich in H_2O and CO_2 at 65°C for 24 hours and the ionic conductivity only decreases by 6.9% to 6.6×10^{-4} S cm^{-1}. Even undergone water-immersion, the LLZT pellet shows good electrochemical stability, which allows an interfacial resistance of 14.6 Ω cm^2 with Li and stable cycling performance of Li|LLZT|LFP cell, exhibiting a high capacity retention of 93% after 100 cycles. Several important features including high relative density, few grain boundaries, water-stable secondary phase of $La_2Zr_2O_7$, and the Li^+-deficient garnet lattice are combined to contribute to the moisture stability as suggested by morphology and surface chemistry analysis and first-principles calculations. This study provides valuable insights into synthesizing fast and moisture-stable lithium garnets in a time-efficient way, which is vital for developing garnet-based ASSLBs.

1. Introduction

Solid-state electrolytes have aroused more and more research interests over recent years aiming at the development of novel all-solid-state lithium batteries (ASSLBs) for portable electronic devices and electric vehicles [1–4]. Among various solid-state electrolytes, lithium-stuffed garnets such as $Li_7La_3Zr_2O_{12}$ (LLZO) are considered as one of the most promising candidates for their outstanding compatibility with lithium anode [5–7]. Significant advances in the LLZO electrolyte have been achieved in the promotion of ionic conductivity (greater than 1 mS cm^{-1}) and the interface engineering to decrease the interfacial resistance between the LLZO and the electrodes [8–12]. Unfortunately, the LLZO is mostly found moisture-sensitive and plagued by the formation of insulating surface impurity layers. The moisture-instability will not only complicate the materials handling during production, storage, and transportation of LLZO, greatly increasing the cost, but also affect the electrode/LLZO interfacial properties because the interface may actually be the electrode/impurity/LLZO structure unless the surficial impurity is carefully removed.

So far, a lot of efforts have been dedicated to understanding the chemistry and the formation of the surface impurity layers in the moisture atmosphere. It is generally believed that the formation of impurities starts with a lithium-proton (Li^+/H^+) exchange reaction, generating lithium hydroxide monohydrate ($LiOH{\cdot}H_2O$) and protonated garnet ($Li_{7-x}H_xLa_3Zr_2O_{12}$) [13,14]. The $LiOH{\cdot}H_2O$ will then react with CO_2 to form Li_2CO_3 on the surface of the garnet electrolyte. Both $LiOH{\cdot}H_2O$ and Li_2CO_3 are poor Li^+ conductors, resulting in an insulating top surface of LLZO after moisture exposure. To deal with the

* Corresponding authors.
E-mail addresses: hxzjy@mail.ustc.edu.cn (X. Huang), hd1@sjtu.edu.cn (H. Duan).
[1] Hongpeng Zheng and Guoyao Li contributed equally to this work.

https://doi.org/10.1016/j.ensm.2022.04.027
Received 13 February 2022; Received in revised form 12 April 2022; Accepted 14 April 2022
Available online 16 April 2022
2405-8297/© 2022 Elsevier B.V. All rights reserved.

moisture-instability, various strategies have been developed, which can be divided into two categories: 1) to inhibit the reaction with moisture by controlling the humidity, optimizing the electrolyte composition by adding a secondary phase and microstructure;[9, 13, 15, 16] and 2) to remove the impurity layer by physical polishing, chemical etching, and heating in controlled atmosphere [17–23]. These strategies either increase the cost and complexity of the synthesis process or are infeasible for future micrometer-thick garnet sheets. Thus, it is highly desirable, from the perspective of material design, to synthesize the garnet electrolyte with good intrinsic moisture stability.

To design a moisture-stable garnet, the following pre-requisites need to be satisfied based on the previous studies. 1) High relative density and small specific surface area. The surface is where the Li^+/H^+ exchange reaction takes place, so the less exposure surface of the pellet the less degree of Li^+/H^+ exchange. The specific surface area is closely related to the relative density; high relative density usually means a small specific surface area. It is also noted that high relative density is necessary to obtain high ionic conductivity and critical current density [24–29]. 2) Few grain boundaries and large grain size. Grain boundaries are more susceptible to moisture than grains due to their higher interfacial energy, so a sample with large grain size and few grain boundaries is desired, which fortunately typically exhibits high relative density and high ionic conductivity [15,26,30]. 3) Controlled secondary phase segregated at grain boundaries. As pointed by Cheng et al. the segregated phase at grain boundaries rich in Al and poor in Li results in limited Li_2CO_3 formation upon air exposure. Li et al. [9] introduces LiF as the secondary phase to decorate the grain boundary and significantly increases the moisture-stability. 4) Moisture-stabile grains. According to the first-principles study, the stability against moisture follows the order $Li_7La_3Sn_2O_{12}$> $Li_7La_3Hf_2O_{12}$> $Li_7La_3Zr_2O_{12}$ under ambient air [31]. Besides, the reaction of Al substituted LLZO with moisture was found not energetically favored [16].

To materialize such a garnet electrolyte meeting the above-mentioned four prerequisites, we need to reconsider and redesign the synthesis route. Solid-state reaction (SSR) is the most widely applied method for the preparation of LLZO and Table S1 summarizes representative SSR conditions. Since its discovery in 2007, LLZO is typically synthesized by an SSR route which involves sufficient grinding of solid precursors in milling solvents (e.g., isopropanol and alcohol) and then annealing or sintering at various temperatures for a long duration with the use of sacrificial mother powders. An excess of lithium salts (10-20 wt.%) is added to compensate for the loss of lithium due to evaporation at elevated temperatures. There are several problems in the typical route: 1) using the milling solvents may cause side-reactions with the starting materials, affect their reactivity during the sintering, and require a long time (more than 12 hours) to dry the powders [32]. 2) The use of excess lithium salts and sacrificial powders not only causes material waste and increases the cost, but also complicates the sintering process in terms of microstructure control and sample placement. 3) The selection of crucible plays an important role in controlling the microstructure of the pellet because the most commonly used Al_2O_3 crucible is reported to react with the garnet pellets at high temperature and the products tend to segregate at the grain boundaries and inhibit the grain growth [33,34]. It is of high interest to develop a low-cost, efficient SSR route to prepare garnet electrolytes with a well-controlled microstructure that can meet the four prerequisites to achieve good moisture stability.

In the present study, we design and synthesize highly densified cubic garnet ceramics with the ultrahigh moisture stability. By design, the garnet-type electrolyte shall possess several important features including high relative density, few grain boundaries, water-stable secondary phase of $La_2Zr_2O_7$, and the Li^+-deficient garnet lattice, which are realized by a solvent-free SSR method. Unlike earlier attempts, the new synthesis route features no use of solvents, no excess lithium salt, no sacrificial powder, and a short sintering time of 10 minutes. The whole period of the synthesis route is reduced to 24 hours after simplifying the process and saving the time for mixing, drying, and annealing. The as-prepared garnet pellets with the well-controlled microstructure exhibit outstanding stability with ambient air, moisture-rich environment, even in water. This work demonstrates the ability to obtain moisture-stable LLZO by tuning the microstructure and provides guidelines for developing low-cost and scalable manufacture for developing garnet-based ASSLBs.

2. Experimental

2.1. Synthesis of garnet-type electrolyte

The cubic LLZT with a nominal composition of $Li_{6.5}La_3Zr_{1.5}Ta_{0.5}O_{12}$ (Ta5Li0) was synthesized via an improved solid-state reaction (SSR) method. Polyurethane (PU) milling jars and yttrium stabilized zirconium oxide (YSZ) balls are dried at 65°C in advance for use. The starting materials were $LiOH{\cdot}H_2O$ (Yonghua, AR), La_2O_3 (Sinopharm Chemical Reagent, 99.95%), ZrO_2 (Sinopharm Chemical Reagent, 99.97%), and Ta_2O_5 (Aladdin, 99.99%). Stoichiometric amounts of these chemicals were weighed and transferred into the milling jar for dry-milled at 175 rpm for 2 hours. The mixed powder and YSZ balls were separated by sieving through the 100-mesh screen and transferred to a 250 mL alumina crucible for pre-sintering at 950°C for 6 hours. The as-sintered precursor powder was dry-milled at 175 rpm for 2 hours. After being sieved through a 200-mesh screen, each 1.0 g powder was uniaxially pressed into green pellets by using a stainless-steel die with a diameter of 12 mm under 500 MPa. The pellets were stacked into the MgO crucible with a diameter of 13 mm, covered without any sacrificial powder but the MgO cover, and sintered at 1320°C for 10 min with a heating rate of 5°C min^{-1}. The obtained pellets were polished by 250 #, 500 #, 1000 #, and 2500 # grit SiC sandpaper to ensure a clean and credible surface, which is critical for moisture-stability and electrochemical tests. Subsequently, the LLZT pellets were transferred into the argon-filled glovebox (H_2O and O_2< 0.1 ppm) to avoid contamination with the air. For comparison, x weight percent of $LiOH{\cdot}H_2O$ as the additional lithium salts was added to prepare the LLZT electrolyte of Ta5Lix series (x = -4, -2, 0, 2, 4, 6, 8) with the same synthesized method. The weights of all the starting materials were listed in Table S2. Additionally, the conventional wet-milling route was employed to synthesize the Ta5Li0 pellets. The synthesis parameters were the same as the solvent-free procedure above expect that we used the isopropanol solvent as the milling media. After wet milling at 175 rpm for 2 hours in a nylon jar, the mixture was transferred to a stainless tray and dried at 65°C for 12 hours.

2.2. Materials characterization

The morphology of the LLZT samples was examined by field emission scanning electron microscopy (SEM, RISE-MAGNA, Czech), equipped with an energy dispersive X-ray spectrometer (EDS) for elemental composition and distribution of the specimen analysis. The phase formation of LLZT samples of Ta5Lix series (x = -4, -2, 0, 2, 4, 6, 8, 20) and the contamination layers after exposure to the humid air were obtained by X-ray diffractometer (XRD, Rigaku; 40kV) with Cu-Kα radiation as the X-ray source in the range of 15~55° and then rechecked at the BL02U2 beamline at the Shanghai Synchrotron Radiation Facility. The relative density of LLZT was measured based on Archimedes' principle. The mass difference of the LLZT pellet before and after immersion in the ethyl alcohol was used to calculate its volume. The relative density equals the mass before immersion divided by the volume and by the theoretical density (5.394 g cm^{-3}. See the theoretical density related to this work in Table S3). Time-of-flight secondary ion mass spectrometry (TOF-SIMS) and TOF-SEM were carried out on a TESCAN Gaia3 FESEM. A TOF-SIMS 5-100 instrument (ION TOF) was attached to the TESCAN GAIA3 FESEM. The three-dimensional surface morphology of LLZT samples was obtained by laser co-focus microscopy (Axio Observer 7, LSM 900) with a 405 nm laser. The optical microscopy (BX51M,

Olympus) was used for the characterization of the morphology of the surface and cross-section for the LLZT pellets.

2.3. Moisture-stability testing

To induce and accelerate Li^+/H^+ exchange of the cubic LLZT in humid air, the pellets were placed in the upper layer of a 65°C steamer for 24 hours which was filled with H_2O and CO_2 vapor (Fig. S7). The lower layer of the steamer contains the supersaturated sodium bicarbonate aqueous solution, which served as the sustaining source of H_2O and CO_2 vapor for Li^+/H^+ exchange reaction and the formation of lithium carbonate on the pellets' surface. Moreover, to verify the stability of Ta5Li0, Ta5Li8, and Ta5Li20 in water, each pellet was immersed in 30 mL deionized water with stirring, and the pH change was recorded with a pH meter within 3 minutes. The immersion-and-pH-recording procedure was repeated several times with fresh deionized water to test the long-term stability of different compositions.

2.4. Cell assembly and testing

The ionic conductivity of the LLZT electrolyte was calculated from data collected by an impedance analyzer (Solartron 1260) in the frequency range from 13 MHz to 1 Hz with an amplitude of 10 mV. Ag|LLZT|Ag cells were assembled by painting the pellets with the conductive silver paint and drying at 65°C for half an hour. For Li|LLZT|Li symmetric cells, the Li electrode was added to the LLZT electrolyte by rubbing the pellets on the molten Li till the Li wets the garnet surface, as reported previously[35]. For full cells, the LLZT pellets were wetted by molten Li on one side, while the other side was attached with a $LiFePO_4$ (LFP) cathode. The preparation of the LFP cathode was as following: the LFP powder was mixed with 10 wt.% Super P conductive carbon black and 10 wt.% PVDF binder in the NMP. This slurry was uniformly spread onto an aluminum foil. The dried LFP cathode was punched into discs with a diameter of 8 mm and the active species loading was about 9.0 mg cm^{-2}. A small amount of electrolyte (~15 μL, 1 mol L^{-1} LiTFSI in a mixture of EC and DMC (volume ratio 1:1)) was added to wet the cathodic interface. All the full cells were assembled in CR2032 coin cells.

2.5. First-principles calculation

All calculations were carried out by using the projector augmented wave (PAW) method in the framework of the density functional theory [36], as implemented in the Vienna *ab*-initio Simulation Package (VASP). The generalized gradient approximation (GGA) and Perdew–Burke–Ernzerhof (PBE) exchange functional was used. Structural relaxation calculations were performed by using the spin-polarized GGA method [37]. The plane-wave energy cutoff was set to 520 eV. The Monkhorst–Pack method [38] with 2 × 2 × 2, 2 × 2 × 2, 2 × 2 × 2, 2 × 2 × 2, 8 × 8 × 8, 8 × 8 × 8 *k*-meshes were employed for the Brillouin zone sampling of $Li_{52}La_{24}Zr_{12}Ta_4O_{96}$, $H_{52}La_{24}Zr_{12}Ta_4O_{96}$, $Li_{50}La_{24}Zr_{12}Ta_4O_{95}$, $H_{50}La_{24}Zr_{12}Ta_4O_{95}$, Li_2O, and LiOH bulks, respectively. The convergence criteria of energy and force calculations were set to 10^{-4} eV/atom and 0.05 eV $Å^{-1}$, respectively. The models of protonated LLZT were performed by substituting hydrogen atoms for selected Li atoms with Pymatgen program.

The Gibbs free energy of H_2O molecular was replaced by the energy of water vapor under the pressure of saturated vapor and corrected with ZPE. using equation (1):

$$G(H_2O,T) = E_{0K}^{DFT} + ZPE + \Delta H_{0\to T} - TS \quad (1)$$

E_{0K}^{DFT} is the calculated energy of an isolated gas-phase molecule using DFT at 0 K. *ZPE* is the zero vibration energy calculated with DFT. $\Delta H_{0\to T}$ is the enthalpy difference for the molecule associated with a temperature change between 0 K and a given temperature T[39]. S is the entropy at temperature T [40]. The Gibbs free energies of solids were approximated as the DFT total energy, $G \approx E_{0K}^{DFT}$.

The driving force of Li^+/H^+ exchange reactions was evaluated by the equation (2):

$$\Delta G = \sum^{G}(\ products) - \sum^{G}(\ reactants) \quad (2)$$

$\sum^{G}(\ products)$ is the Gibbs free energies of all products, and $\sum^{G}(\ reactants)$ is the Gibbs free energies of all reactants.

3. Results and discussion

3.1. Design of garnet pellets with ultrahigh air stability

A typical solid-state-reaction (SSR) route based on wet milling to synthesize garnet-type electrolyte is shown in Fig. 1. The first step is to mix the raw materials with 10-20 wt.% of excess lithium salt by wet milling. Isopropanol (IPA) is widely chosen as the solvent at this step for its relatively low polarity and small solubility to $LiOH{\cdot}H_2O$ which prevents the severe Li^+/H^+ exchange [7,32,41]. The use of the solvent generally requires more than 12 hours to thoroughly dry the powders at about 70°C and sieving, which is necessary after each wet milling [24,42-44]. Then the powers are pre-sintered at 900°C or 950°C for at least 6 hours to obtain the garnet phase [29,45-47]. A second-time wet milling is followed to tailor the particle size and obtain a large specific surface area which provides densification driving force in the final sintering step [30,44]. During the final sintering step, adequate amounts of sacrificial mother or bed powders are adopted to cover or to lay beneath the green pellets to supplement the lithium loss during the high-temperature (over 1100°C) and long-time (from 6 to 36 hours) sintering as listed in Table S1. This route normally takes 3 days to prepare one batch of electrolytes.

To increase the efficiency and scalability of the above route, here we design a new synthesis route: use no solvents, no excess lithium salt, or no sacrificial powder, and shorten the sintering duration at 1320°C to 10 min (Fig. 1b). Since the dry-milled particles tend to stick to the wall of the nylon jar, a smooth poly-urethane (PU) jar is used instead, which enables effective milling and a high recovery rate of the powder. The elimination of the use of solvents dispels the possible concerns about the toxicity and recovery of the solvents. Meanwhile, using no solvent saves a considerable amount of time spent in drying the powder and cleaning the experimental apparatus, which is of significance to the mass manufacture of the garnet electrolyte. As a result, the time of the whole process is shortened to 24 hours.

The as-prepared Ta5Li0 samples by both routes have been evaluated in terms of phase formation (Fig. 1c), cross-sectional morphology (Fig. 1d), and ionic conductivity and relative density (Fig. 1e). For the Ta5Li0 pellet synthesized via the conventional route, a detectable amount of the impurity phases, Li_2ZrO_3 and $La_2Zr_2O_7$, is observed (Fig. 1c), which indicates the loss of Li_2O during sintering [34,48]. As shown in Fig. 1d, the pellet displays pure white and insignificant shrinkage after sintering; the morphology shows many pores within the pellets, implying that the Li_2O loss and impurity formation may inhibit the grain growth and the densification process [26]. Fig. 1e indicates that the pellet exhibits a low ionic conductivity ($0.5\pm0.08 \times 10^{-4}$ S cm^{-1}) and low relative density (81.1%. See the theoretical density in Table S3), therefore lacking practical applicability. After storing it in air environment with an average relative humidity of 45-65% for four months, the ionic conductivity decreased to $0.1\pm0.05 \times 10^{-4}$ S cm^{-1}.

In comparison, the Ta5Li0 pellet possesses a cubic phase (Fig. 1c) with much less $La_2Zr_2O_7$ secondary phase even though no excess lithium salt is used. This, to our best knowledge, is the first work demonstrating such high-quality garnet pellets by an SSR route without excess lithium salt or sacrificial powder. Fig. 1d shows that Ta5Li0 pellet represents ceramic lustre and high shrinkage; from the cross-sectional SEM image, only a small quantity of grain boundaries and negligible pores can be

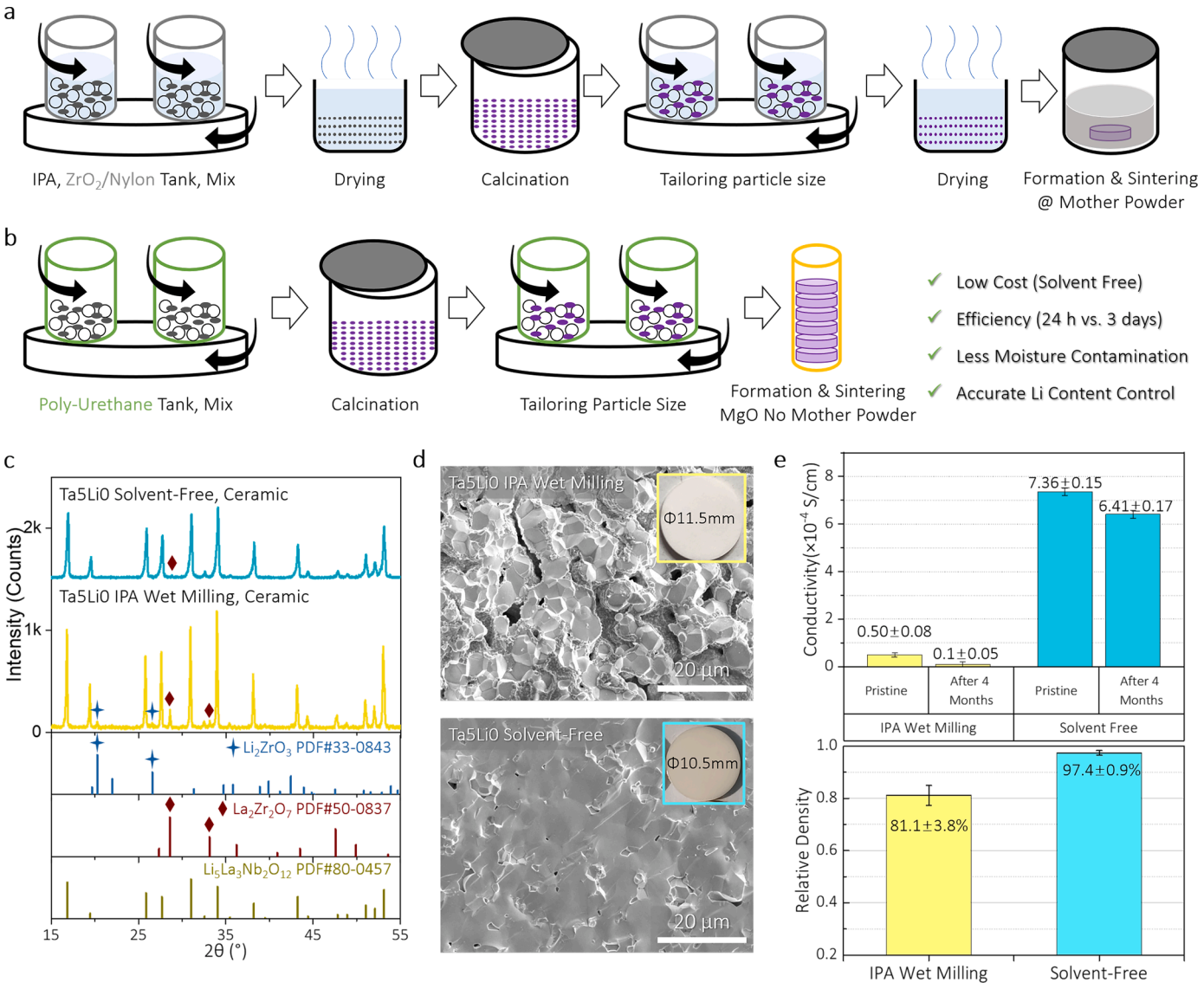

Fig. 1. Comparison of $Li_{6.5}La_3Zr_{1.5}Ta_{0.5}O_{12}$ electrolyte (Ta5Li0) synthesized by conventional wet-milling and solvent-free routes. a) Schematic diagram of the conventional wet-milling route. b) Schematic diagram of the modified solvent-free route. c) Powder XRD pattern of the Ta5Li0 electrolyte and the standard PDFs of the possible phases. d) Cross-sectional SEM images of the Ta5Li0 pellets. e) Ionic conductivity (see the EIS spectra in Fig. S1) and relative density of the as-sintered Ta5Li0 pellets prepared by these two routes.

observed, and the grains in the view tend to grow into one whole grain (Fig. S3). The Ta5Li0 pellet achieves the high ionic conductivity (7.36 $\pm$0.15 $\times$ 10^{-4} S cm^{-1}) and relative density (97.4%) (Fig. 1c). The ionic conductivity decreases to 6.41$\pm$0.17 $\times$ 10^{-4} S cm^{-1} after four-month storage in ambient environment.

There are several important differences between the wet and dry methods. The first one is no use of solvent. Protic solvents including isopropanol with readily available −OH functional groups may induce lithium/proton exchange, thus causing the irreversible lithium loss of the pristine materials [32]. Moreover, the high surface tension of the solvent may cause the powder agglomeration and affect the reactivity of the particles, subsequently impacting the microstructure of LLZT electrolyte [24,49-51]. Second, no excess lithium salt or sacrificial powder is used. Because the dry milling produces highly reactive dry powders with no lithium loss, sintering duration at a high temperature can be shortened to 10 min and Ta5Li0 with high ionic conductivity and cubic garnet phase is still obtained. This simplifies the processes and cuts the material cost. Third, the MgO crucible plays a critical role in manipulating the lithium concentration during 1320°C sintering. Using MgO crucible prevents possible side reactions between the sample and the widely-used alumina one, whose products segregate at the grain boundaries [16,33,44]. Moreover, the shape of the crucibles (Fig. S2) perfectly fits the stack of green pellets, which further suppresses Li_2O evaporated in a limited space. Taking the whole preparation process into consideration, including mixing, calcination, formation, and sintering, the period of the solvent-free route could be shortened within 24 hours (see details in Experimental section), compared with three days in a typical wet-milling route. The stoichiometric LLZT electrolyte synthesized via this newly designed approach is of quality comparable to those prepared by other costly techniques such as spark plasma sintering (SPS) and hot pressing [52–54].

3.2. *Enhanced moisture stability by tuning lithium contents*

To study the effect of Li_2O content in the LLZT electrolyte on the moisture stability, a series of LLZT pellets with different lithium contents in the raw materials, named after Ta5Li−4, −2, 0, 2, 4, 6, 8, have been prepared via the solvent-free method (see details in Fig. S4). Powder X-

ray Diffraction (Fig. 2a) is carried out to verify the phase formation of the LLZT electrolyte. It is found that pure cubic phase could be achieved only when the Li_2O content is more than the stoichiometric composition of $Li_{6.5}La_3Zr_{1.5}Ta_{0.5}O_{12}$ in the raw materials, including Ta5Li2 to Ta5Li8. Once the lithium source is insufficient at the initial stage, the secondary phase $La_2Zr_2O_7$ will appear in Ta5Li−2 and Ta5Li−4 [48,55,56]. Besides, the characteristic diffraction peaks of La_2O_3 are also detected from Ta5Li−4, indicating that further decreasing lithium content resulted in the residual of impurity phases such as La_2O_3, which is similar to the low-temperature solid-state route [57–60].

Ionic conductivity and relative density of the LLZT pellets with different lithium contents are determined and summarized in Fig. 2b and c. Fig. 2b shows the Nyquist plots of the LLZT samples normalized by the geometry of the pellet from Ta5Li−4 to Ta5Li8. The impedance plots

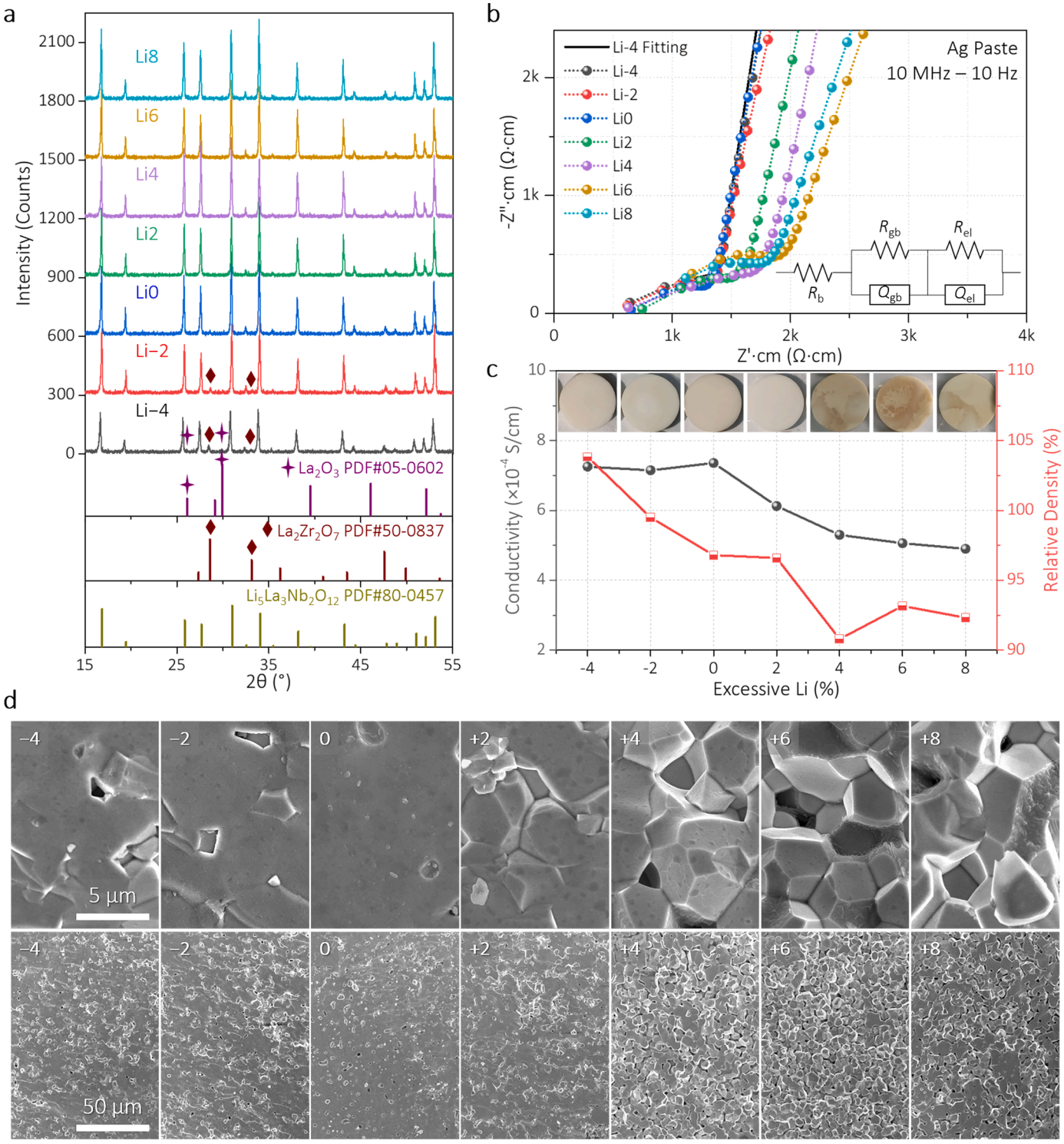

Fig. 2. Characterization and Measurement of LLZT with different lithium contents (ranging from −4% to 8%). a) Powder XRD pattern of the LLZT electrolyte and the standard PDFs of the possible phases. b) EIS spectra of the as-sintered LLZT pellets at room temperature in dry air, with silver as blocking electrode. The inset presents the equivalent circuit. c) Conductivity and relative density of the LLZT pellets. The inset displays images of the as-synthesized LLZT pellets. d) Cross-sectional SEM images of the LLZT pellets.

consist of one suppressed semicircle and an inclined tail, which can be attributed to the total (bulk and grain boundary) contribution and the blocking effect of the Ag electrode. The solid line represents the fit to the experimental data based on the equivalent circuit consisting of $R_b(R_{gb}//CPE_{gb})(R_{el}//CPE_{el})$ elements using the ZSimpWin program, where R is the resistance, CPE is the constant phase element and the subscript b and gb refers to the bulk and grain-boundary contribution, respectively. The room-temperature ionic conductivity of the LLZT is determined to be 7.253×10^{-4} S cm^{-1}, 7.148×10^{-4} S cm^{-1}, 7.357×10^{-4} S cm^{-1}, 6.126×10^{-4} S cm^{-1}, 5.3×10^{-4} S cm^{-1}, 5.06×10^{-4} S cm^{-1}, and 4.9×10^{-4} S cm^{-1} from Ta5Li−4 to Ta5Li8, respectively. The ionic conductivity maintains constant for Ta5Li−4, −2, and 0, meaning that a small amount of secondary phase (i.e., $La_2Zr_2O_7$ or La_2O_3 in Fig. 2a) has little effect on the lithium-ion transport. As shown in Fig. 2c, the relative density follows a similar trend as the ionic conductivity, decreasing from close to 100% for Ta5Li−2 to 92.5% for Ta5Li8. The heavy secondary phases like $La_2Zr_2O_7$ (6.12 g cm^{-3}) and La_2O_3 (6.52 g cm^{-3}) enable the relative density of the pellet to even excess 100% of the LLZT theoretical density (5.394 g cm^{-3}) for Ta5Li−4.

Fig. 2d displays the effect of Li_2O content on the morphology of the LLZT electrolyte. The number of the grain boundaries is distinctly increasing, some of the grain surfaces even become rough, and more inter-grain matter forms with the increasing lithium content. To characterize the inter-grain matter, the Ta5Li20 pellet was synthesized and subject to EDS. As shown in Fig. S5, EDS line scanning starts from a large grain, via the rough substance to be determined, a small grain, and ends at another inter-grain matter. Clearly, the element signals of the grain are mainly contributed by La and Zr, while that of the inter-grain matter is basically from O, indicating their completely different composition. To determine the lithium distribution within the sample, the cross-section of the Ta5Li20 pellet was examined by TOF-SIMS. As shown in Fig. S6, the lithium element is visually concentrated at the grain boundaries. Together with the EDS data, we can conclude that the excess lithium salt will remain in the form of lithium oxide at the grain boundaries.

Fig. 2 as a whole suggests that the decrease in conductivity with increasing lithium contents can be attributed to the following reasons: (1) phase formation, (2) porosity, and (3) grain boundary chemistry [52,61,62]. The more the excess lithium contents, the more the pores and lithium-ion-insulating secondary phases like lithium oxide existing in the pellet. Considering the phase formation, the ionic conductivity, and the morphology, the stoichiometric LLZT (Ta5Li0) synthesized via the solvent-free route is determined to have the best performance. Owing to its dense microstructure, high purity, and chemical stoichiometry, Ta5Li0 is expected to possess good moisture-stability in ambient air.

High moisture-stability is crucial for the solid-state electrolyte because it determines whether electrolyte is possible to be produced and stored in ambient air. Previous research suggested that the garnet-type electrolyte is sensitive to moisture because a Li^+/H^+ exchange reaction will take place and form a Li_2CO_3 surficial impurity layer, severely impacting the electrochemical performance of the electrolyte [13,63-65]. In this work, we designed a particular steamer (see details in Fig. S7) that provides an atmosphere rich in H_2O and CO_2 for the Li^+/H^+ exchange reaction to occur. Compared with the pre-existing studies on moisture-stability (summarized in Table S5), this atmosphere in the steamer is much more severe for the LLZT electrolyte in terms of the vapor pressure of water and testing temperature (25.3 kPa at 65°C vs 3.12 kPa at 25°C). Here, LLZT pellets of three compositions, Ta5Li0, Ta5Li8, and Ta5Li20 prepared via the solvent-free method, were chosen to be tested in such an environment to investigate the effect of the excess lithium salt on the moisture-stability.

To eliminate the influence of the surface roughness, all the pristine pellets underwent the same polishing process, and the roughness was characterized using the laser co-focus microscopy. As shown in Table S4, the root-mean-square roughness of the pristine LLZT pellets is in the range of 3.014-5.147 μm after polishing with the #2500 grit SiC sandpaper. After storing in the steamer at 65°C for 24 hours, the roughness increases to 3.671, 9.192, and 23.33 μm for Ta5Li0, Ta5Li8, and Ta5Li20, respectively. The optical microscopy (OM) images (Fig. 3a) and the reconstructed laser co-focus microscopy image (Fig. 3b) show that the pellets of different excess lithium exhibit various degrees of morphology change. For the Ta5Li0 pellet, the as-polished surface is rather smooth. After 24-hour exposure, there appear few visible humps in the optical photo, and the scratches of the polishing can be dimly seen. Very limited impurities are scattered on the surface from the cross-sectional OM images. In contrast, for Ta5Li8, and Ta5Li20, more and larger impurity particles (Fig. 3a) grow on the pellet surface after the steaming test, leading to a rougher surface than Ta5Li0 (Fig. 3b). The polishing scratches are indistinct for both compositions since the pellet surfaces seem fully covered by an impurity layer, which can be distinguished from the LLZT bulk according to their refraction of light indicated by the dotted line in the cross-sectional view (Fig. 3a).

The conductivities of the pellets before and after the steaming test are determined by the impedance measurements and the results are shown in Fig. 3c and Fig. S9. After the moisture-tolerance test, the ionic conductivity of the Ta5Li0 pellet decreases from 7.1×10^{-4} S cm^{-1} to 6.6×10^{-4} S cm^{-1}, decreasing by 6.9%. Whereas for Ta5Li8 and Ta5Li20, the ionic conductivities of the pristine samples are 6.8×10^{-4} and 6.6×10^{-4} S cm^{-1}, respectively. After the steaming test, the EIS spectra of Ta5Li8 and Ta5Li20 pellets lose the characteristic semicircle, suggesting that the impurity formation severely impeded the lithium-ion transport for Ta5Li8 and Ta5Li20 pellets.

To further explore the conductivity degradation of the LLZT pellets, the distribution of relaxation times (DRT) analysis is employed, where the impedance data are transformed from the frequency to time domain such that peaks associated with characteristic time-constants can be identified [66–68]. The DRT analysis results are shown in Fig. 3d. The time constants and peak intensity of the characteristic peaks given out by DRT are listed in Table S6. Based on the literature, the peaks (peak 1) with small time-constants (i.e. smaller than 10^{-7} s) are associated with the ionic conduction of the lattices inside grains; those (peak 2) with medium time-constants (i.e. in the range of 10^{-7}~10^{-4} s) are associated with the ionic conductivity of the grain boundaries; and those (peak 3) with large time-constants (i.e. slower than 10^{-4} s) can be attributed to the non-ideal capacitive behavior of the Ag-LLZT interfaces and the blocking electrodes [69,70]. Stronger peaks usually shift to larger characteristic time constants and mean smaller conductivity. As shown in Fig. 3d, before the steaming test, Ta5Li0, Ta5Li8, and Ta5Li20 exhibit small peak 1 with the time-constant of 7-8 $\times 10^{-8}$ s, corresponding to the fast Li^+ migration in the Wyckoff *96h* ↔ *24d* ↔ *96h* route [70]. While Ta5Li0 possesses a single peak 2 with the time constants in the range of 10^{-7}~10^{-4} s, Ta5Li8 and Ta5Li20 have multiple peaks in this region. The appearance of the side peaks (i.e., 2a, 2b, 2c) may arise from the abnormal morphology (i.e., many grain boundaries in Ta5Li8) as shown in Fig. 2d and the existence of undesirable impurities like Li_2O at the grain boundaries [70]. After the steaming test, there is little change for the peak 1 of Ta5Li0 and Ta5Li8, while the intensity of the peak 1 of Ta5Li20 increases from 466 Ω to 5163 Ω. More interestingly, the intensity of the peak 2 of Ta5Li0 increases from 990 Ω to 3445 Ω. For Ta5Li8 and Ta5Li20, the side peaks, 2a, 2b, and 2c, become much stronger with higher time constants, suggesting the significant increase of the grain boundary resistance of the solid electrolyte after the steaming tests [69]. The increasing grain boundary resistance is related to the formation of the surficial impurities (e.g. Li_2CO_3 and $LiOH{\cdot}H_2O$), as indicated by the XRD in Fig. S10 [13,63]. It has been proposed that the impurity formation starts with the Li^+/H^+ exchange reaction and the Li^+/H^+ exchange reaction preferentially tends to occur at the grain boundaries. [26]

As discussed above, the excess lithium contents in Ta5Li8 and Ta5Li20 will lead to more grain boundaries and more lithium oxide at the grain boundaries in the pellets than in Ta5Li0. Both factors facilitate the Li^+/H^+ exchange reaction and the accumulation of impurities,

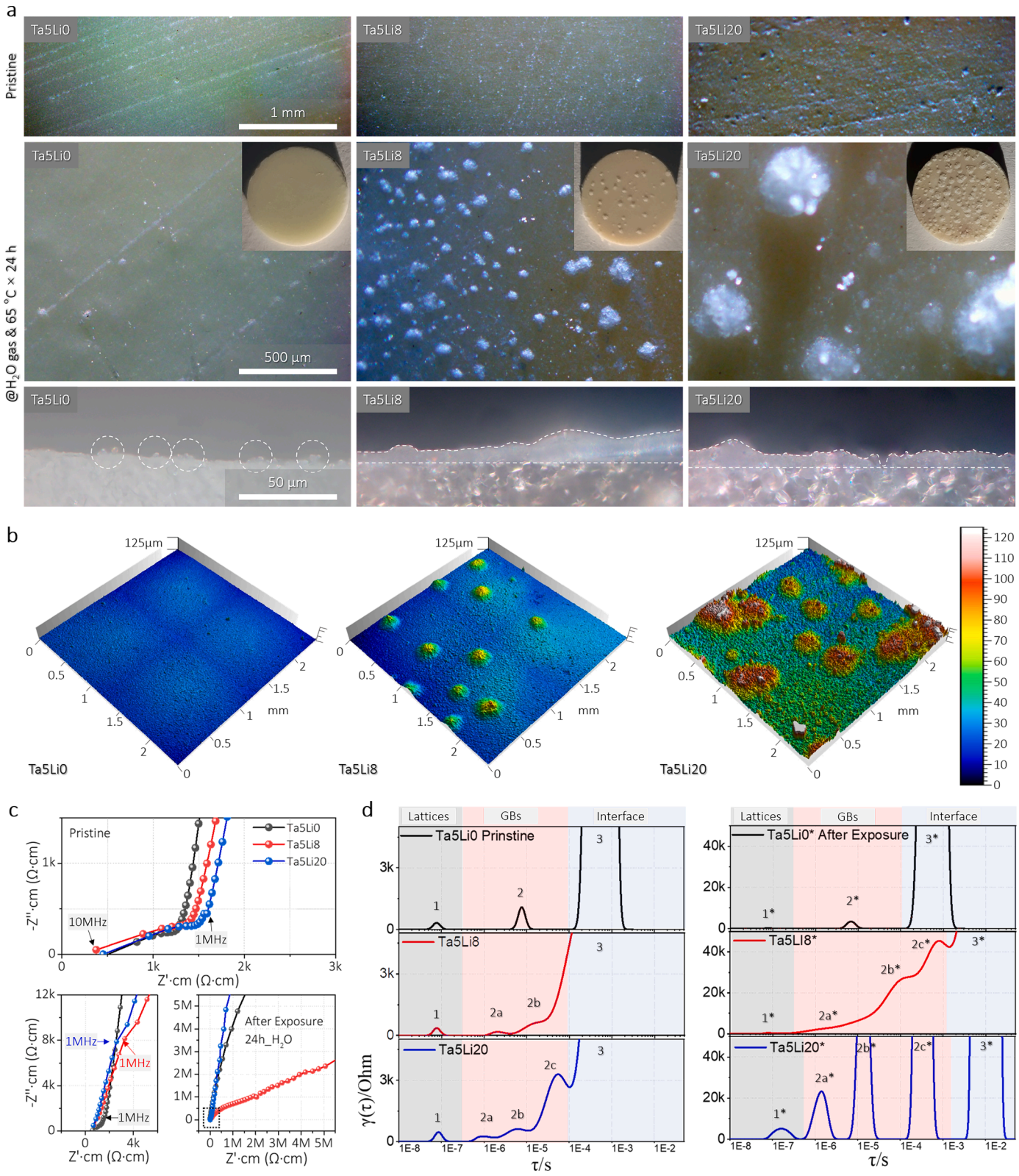

Fig. 3. Moisture-tolerance test of LLZT pellets (Ta5Li0, 8 and 20) in an atmosphere rich in H_2O and CO_2 at 65°C for 24 hours. a) Optical microscopy images of the samples before (front surface, the first row) and after (front surface, the second row; cross-section, the third row) the test. The inset displays images of the exposed pellets. b) Laser co-focus microscopy images (3D reconstructed, 2.5 mm × 2.5 mm) of the front surface after the test. c) EIS spectra of the LLZT pellets before (the top) and after (the bottom) the test, measured at room temperature in dry air, with silver as blocking electrode. d) Distribution functions γ(τ) of the EIS spectra in figure c. The superscript * refers to the moisture-treated LLZT pellets.

resulting in low moisture stability and the conductivity degradation in Ta5Li8 and Ta5Li20. Besides, the impediment to Li^+ migration in the grains observed in Ta5Li20's peak 1 also caught our attention and the water-immersion test was thus designed as followed to explore the influence of the grain boundary chemistry but also the grain.

3.3. Water immersion tests of the ultrahigh stable pellets

To evaluate the effect of the excess lithium salt on the water stability, Ta5Li0, Ta5Li8, and Ta5Li20 were subject to an immersion test in the deionized water. When the LLZT pellet is immersed into the deionized water with a starting pH value of 6.0, the grain boundary impurities such as Li_2O can dissolve instantly and change the morphology of the pellets and the pH value of the solution. Fig. 4a and Fig. S11 show the surface morphology after the immersion test. Obviously, from Ta5Li0 to Ta5Li20 with increasing lithium content, severe erosion and numerous pits occur on the pellet surfaces, which are consistent with the results of the steaming test. Fig. 4 brecords the dynamic change of the pH value of the deionized water. As shown in Fig. 4b and Video S1-3, once the pellets are put into the water, the pH value sharply increases at first, then gradually reaches a plateau within ~30 s. The stabilized pH values of the Ta5Li0, Ta5Li8, and Ta5Li20 are 7.7, 9.2, and 10.5, respectively, corresponding to the dissolved lithium concentrations of 4.0×10^{-7}, 1.58×10^{-5}, and 3.2×10^{-4} mol L^{-1}, suggesting that the Ta5Li0 has the least degree of lithium salt dissolution and best water stability. Besides, the immersion tests are repeated multiple times, and the stabilized pH values are displayed in Fig. 4c. As shown in Fig. 4c, the pH values for Ta5Li0 and Ta5Li8 remain close to 7 in the subsequent immersion, suggesting that the surficial Li_2O in Ta5Li8 has completely dissolved in the first immersion test. Whereas for Ta5Li20, the pH value is still over 9 after 5-time immersion, indicating that the dissolution is far from completion. It should be noted that the immersion of Ta5Li0 only

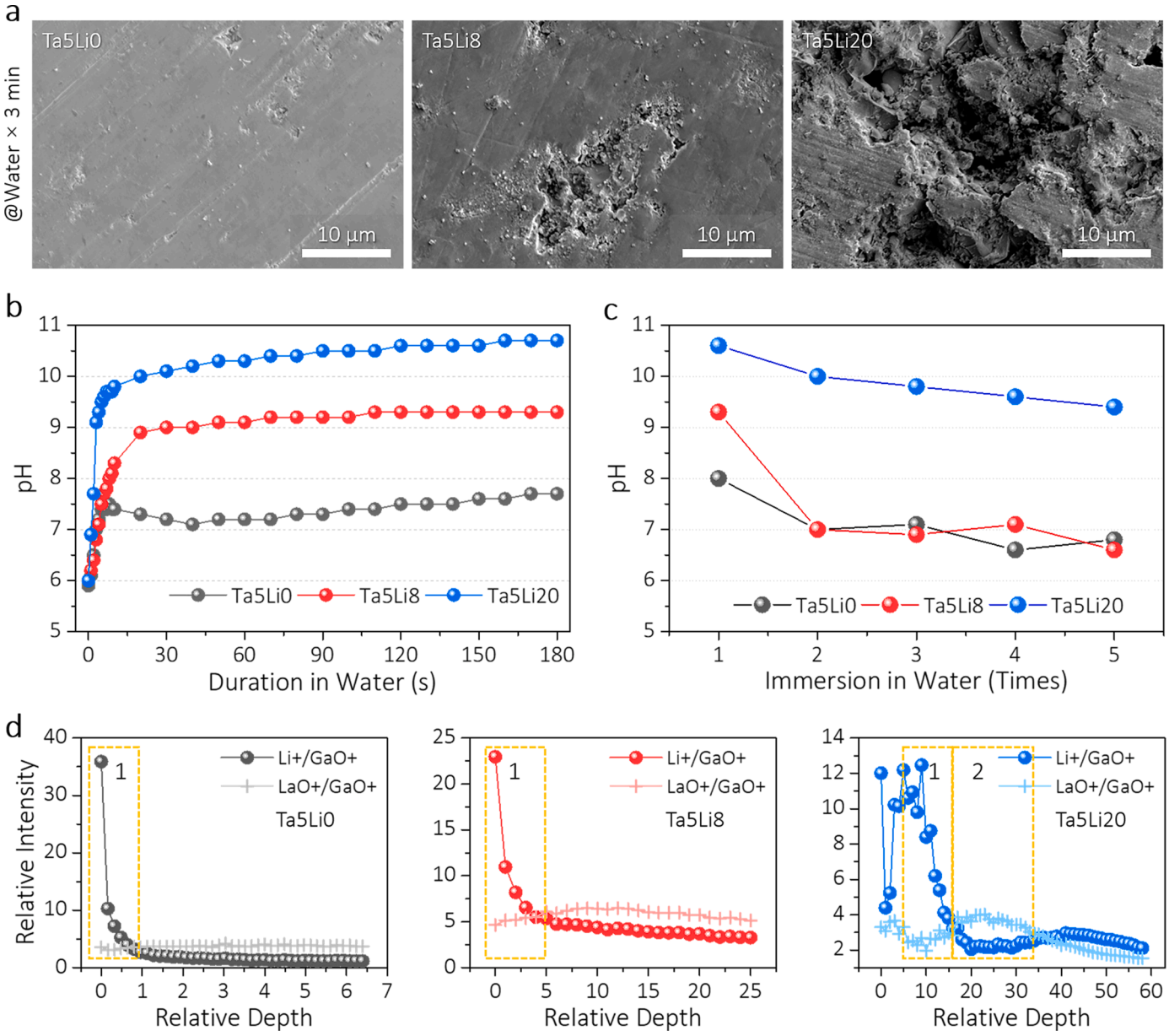

Fig. 4. Water-immersion test of LLZT pellets (Ta5Li0, 8 and 20) in the deionized water (30 mL, initial pH 6.0) at room temperature for 3 minutes. a) SEM images of the LLZT pellets after the immersion. b) Change in pH versus time in the first immersion. (See details in Video S1-3). c) Change in pH versus the number of immersions. The deionized water was replaced with fresh one for each 3-minute immersion. d) FIB-SIMS depth profiles using a 7 nA primary ion beam current on the LLZT pellets after the immersion. All the intensity was given as a ratio to the $69Ga^+$ intensity.

increases the pH value of the DI water from 6.0 to 7.7 during the first immersion and barely changes the pH value in the subsequent immersion tests, highlighting the great water-stability of the Ta5Li0 synthesized by the present solvent-free method.

After the 3-minute immersion test, the pellets were dried in a vacuum oven and characterized by TOF-SIMS depth-profiling to perform an in-depth chemical analysis. A small analysis crater size (5 μm × 5 μm) is used so that all analyses were performed within the grains with no contributions from the grain boundaries, verified by the morphology inspection in Fig. S12. To correct the effects of the surface roughness and morphology change during sputtering on the secondary ion signals, the secondary ion intensities are normalized to the $^{69}Ga^+$ secondary ion intensity, so the relative intensities are given. As the sputtering region and the current of $^{69}Ga^+$ ion source are kept the same in all the tests, the intensity versus time can be transformed into versus the relative depth. As shown in Fig. 4d, the $^7Li^+/^{69}Ga^+$ ratio of the Ta5Li0 drops dramatically with a slight increase of the $^{155}LaO^+/^{69}Ga^+$ ratio within a relative depth of 1 indicated as the dotted box #1. The Ta5Li8 exhibits a similar trend except that the relative depth increases to 5. In contrast, Ta5Li20 shows a very different profile: the $^7Li^+/^{69}Ga^+$ ratio decreases dramatically in the first box (a relative depth of 17) and increases gradually in the second box (a relative depth from 17 to 35) before reaching a plateau region that is the pristine bulk LLZT. As suggested by Brugge et al. the sharp decrease of the $^7Li^+/^{69}Ga^+$ ratio (box #1) can be attributed to the Li^+/H^+ exchange at the surface, producing LiOH rich in Li^+; box #2 is associated with the formation of an H-LLZT region, where the diffusion of H^+ and Li^+ occurs [14]. After the water treatment, there are two possible origins of the Li^+-rich LLZO surface: the continuous H^+/Li^+ exchange during drying and during sample transfer in the air to the TOF-SIMS instrument [14]. Interestingly, for Ta5Li0 and Ta5Li8, box #2 is almost absent, implying no sign of the formation of the H^+/Li^+ diffusion layer by reducing the excess lithium salt. The grain of Ta5Li0, in particular, shows the best water-stability with the least relative depth of 1 among these three compositions.

To further investigate the application of the water-immersed pellets, Li|LLZT|Li symmetric cell and Li|LLZT|LFP batteries were assembled and tested. Ta5Li0, Ta5Li8, and Ta5Li20 pellets were immersed in deionized water for 3 minutes, dried in a vacuum oven, and wetted by molten lithium metal by the same means used before. [35] Fig. 5a shows the impedance plots of the Li symmetrical cells and the interfacial resistance can be obtained by fitting the equivalent circuits. Ta5Li0 and Ta5Li8 have a smaller interfacial resistance of 14.6 and 43 Ω cm^2, respectively. Whereas the interfacial resistance for Ta5Li20 is much larger (2580 Ω cm^2), indicating that the Li^+/H^+ exchange and moisture erosion have caused the invalid contact with lithium and hindered the lithium-ion transfer at the interface as shown in Fig. S14.

The Li|LLZT|LFP batteries were cycled with the cut-off voltage in the range of 2.5 V-3.8 V at 0.5 C (0.765 mA cm^{-2}) at 60°C. The LFP cathode has an active species loading of 9.0 mg cm^{-2}, which is higher than that reported to be assembled with the lithium garnet electrolyte. [71–75] Fig. 5c compares the charge/discharge voltage profiles of the Li-LFP batteries at the 1st, 33rd, 50th and 100th cycles. LFP|Ta5Li0|LFP shows excellent cyclic behavior with typical charge/discharge curves with a flat plateau at ≈3.5 V. At 0.5C rate, the discharge capacity retention for the 1st, 33rd, 50th, and 100th cycles were 168.7 mAh g^{-1}, 158.5 mAh g^{-1}, 157.7 mAh g^{-1}, and 158.1 mAh g^{-1}, respectively as shown in Fig. 5b.

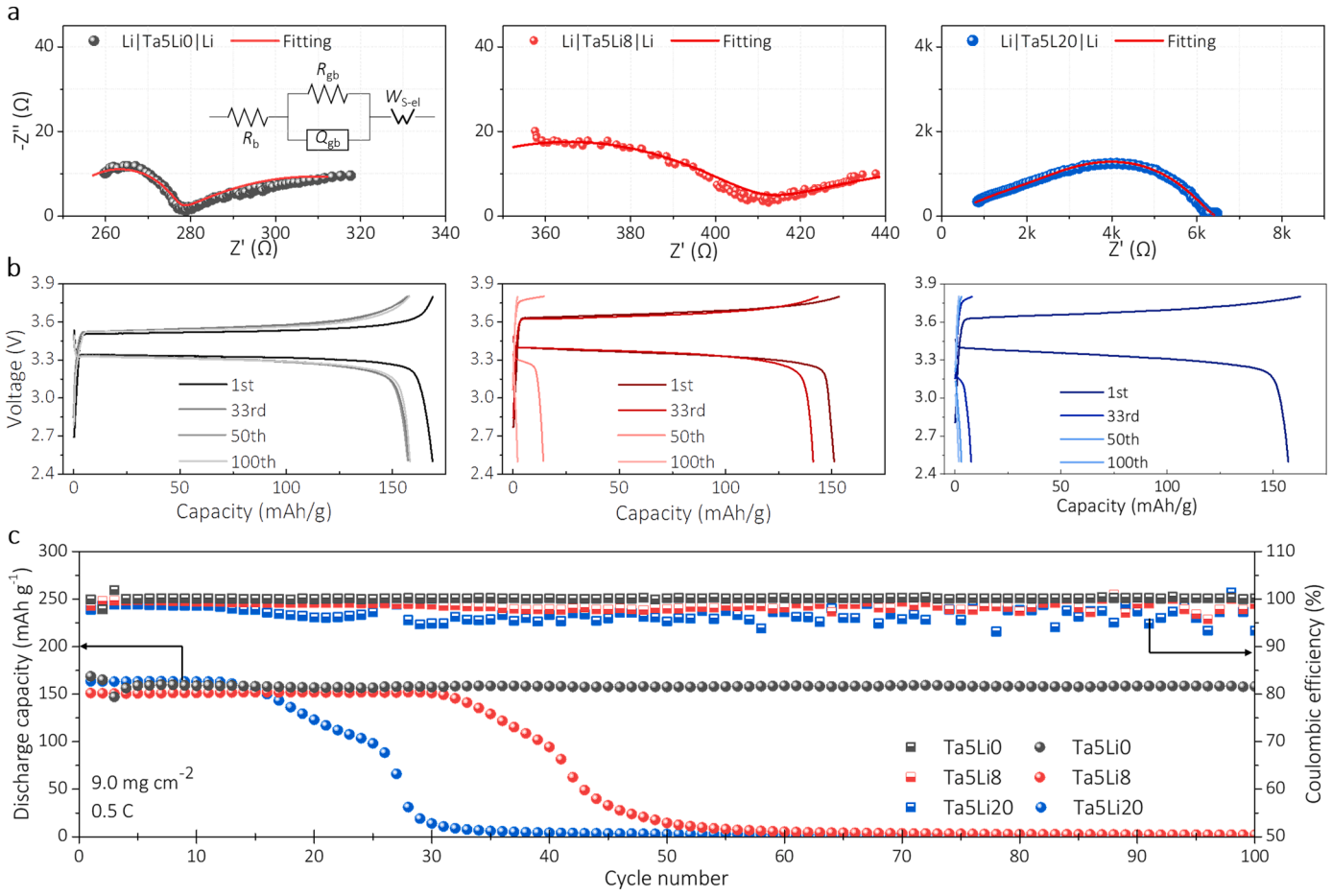

Fig. 5. Electrochemical performance of the cell assembled with the LLZT pellets (Ta5Li0, 8 and 20) after 3-minute deionized-water treatment. a) Nyquist plots for EIS spectra of Li|LLZT|Li symmetric cells at room temperature. b) Voltage profiles of Li|LLZT|LFP batteries at different cycles of the 1st, 33rd, 50th, and 100th at 60°C. c) Cycling performance of Li|LLZT|LFP batteries for 100 cycles at 0.5 C at 60°C.

Even after 100 cycles, the capacity retention rate was more than 93% of the initial capacity. The Li|Ta5Li0|LFP clearly shows the greater initial capacity and initial coulombic efficiency (168.7 mAh g^{-1} and 99.91%) than those of Ta5Li8 (161.4 mAh g^{-1} and 98.52%) and Ta5Li20 (163.7 mAh g^{-1} and 98.68%), kept well in the subsequent cycles with a small polarization voltage. Whereas for Ta5Li8 and Ta5Li20, the polarization voltage was raised in the subsequent cycles, accompanied by the rapid degradation of the discharge capacity. Fig. 5e shows the columbic efficiency and discharge capacity for each cycle. The Li|Ta5Li0|LFP battery maintains 158.1 mAh g^{-1} discharge capacity and close to 100% columbic efficiency even at the 100th cycle. In contrast, the discharge capacity of the battery assembled with water-immersed Ta5Li8 and Ta5Li20 falls below 100 mAh g^{-1} after the 40th and 25th cycle, respectively. It follows then that the LLZT pellet with the high moisture tolerance is crucial for good interfacial contact and excellent electrochemical cycling.

3.4. Mechanism investigation and outlook

Among the various compositions of the LLZT electrolyte, Ta5Li0 exhibits remarkable moisture-resistance, in both steaming tests and water-immersion tests. The powder XRD was used to characterize the crystal structure of the LLZT electrolyte with different lithium contents. As shown in Fig. 6a, the characteristic peak around 16.8° of cubic garnet moves to a low diffraction angle with an increasing amount of Li contents, suggesting the expansion of the lattice parameters according to the Braggs' rule. This trend is rechecked by the synchrotron-based XRD measured with BL02U2 beamline at SSRF (Fig. S13). When the lattice contains more lithium atom in garnet-type electrolyte, the lattice parameters are also reported to be larger [76,77].

To further understand the moisture-stability of the LLZT lattice, we conducted the first-principles calculation to compare the Gibbs free energy of the chemical reaction between H_2O and possible chemical compositions in LLZT. Specifically, we select the secondary phases including Li_2O and $La_2Zr_2O_7$, the stoichiometric LLZT as well as LLZT (-Li_2O) whose crystal cell lacks one formula of Li_2O and compare the Gibbs free energy change of the reactions:

$$Li_2O(s) + H_2O(g) \rightarrow 2LiOH \tag{3}$$

$$\frac{1}{52}Li_{52}La_{24}Zr_{12}Ta_4O_{96}(s) + H_2O(g) \rightarrow \frac{1}{52}H_{52}La_{24}Zr_{12}Ta_4O_{96}(s) + LiOH(s) \tag{4}$$

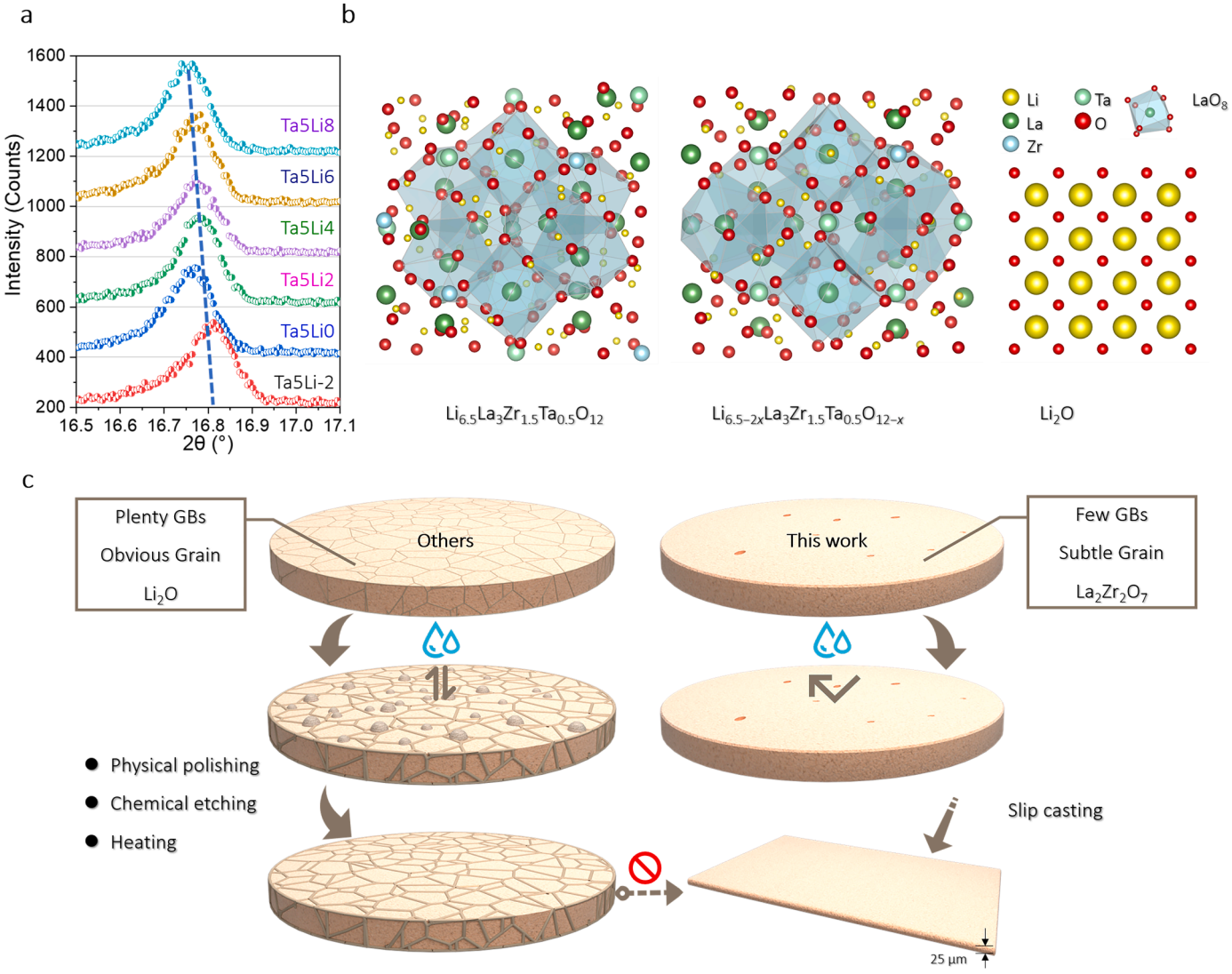

Fig. 6. Mechanism analysis of the moisture stability of LLZT pellets. a) Powder XRD pattern of the pristine LLZT electrolyte with 2θ in the range of 16.5~17.1°. b) Atomic structure of the computational cells for $Li_{52}La_{24}Zr_{12}Ta_4O_{96}$ and Li-deficient $Li_{50}La_{24}Zr_{12}Ta_4O_{95}$. c) Schematic illustration of the microstructure of the conventional moisture-sensitive garnet pellets and the moisture-stable pellets in this work.

$$\frac{1}{50}Li_{50}La_{24}Zr_{12}Ta_4O_{95}(s) + H_2O(g) \rightarrow \frac{1}{52}H_{52}La_{24}Zr_{12}Ta_4O_{95}(s) + LiOH(s) \quad (5)$$

The calculated models are shown in Fig. 6b and the calculation results are compiled in Table S7. Obviously, the Gibbs free energy of reaction (3) is −1.3173 eV per Li, close to the experimental value reported by Chase et al. [78] This implies that Li_2O can spontaneously react with H_2O while $La_2Zr_2O_7$ is nonreactive as there are no reasonable products. Moreover, the Gibbs free energy increases from −0.6200 eV to −0.5769 eV when the stoichiometric $Li_{52}La_{24}Zr_{12}Ta_4O_{96}$ ($Li_{6.5}La_3Zr_{1.5}Ta_{0.5}O_{12}$) goes to Li-deficient $Li_{50}La_{24}Zr_{12}Ta_4O_{95}$, indicating that the Li-deficient lattice has a lower possibility of being protonated and thus is more moisture-stable than the Li-rich LLZT. Since excess Li usually results in Li_2O at the grain boundary and Li-rich lattice, the calculation results well explain, from the perspective of the secondary phase at the grain boundary and the lattice itself, the outstanding moisture-stability of the Ta5Li0.

The schematic diagram (Fig. 6c) summarizes the microstructure of the conventional moisture-sensitive garnet pellets and the moisture-stable Ta5Li0 pellets in this work. Microstructure is one of the major factors affecting the moisture-stability as discussed below. The Ta5Li0 possesses large and subtle crystalline grains with few grain boundaries and some close pores within the sample; whereas the conventional LLZT with excess Li shows obvious grains with plenty of grain boundaries, and the excess lithium salts may aggregate in the form of lithium oxide at the grain boundaries. Such residual lithium oxide tends to induce the hydration process and becomes the weak point facing the attack of moisture. After air exposure, impurity phases including Li_2CO_3 and $LiOH{\cdot}H_2O$ tend to form at these weak points, as shown in Fig. 3c. Besides, as the lithium occupation sites in the LLZT crystal cell are fractional, the excess lithium salt is presumed to embed into the lattice and change the lattice parameter, which affects the lattice reactivity with water molecules. [76,79] In the form of pellets with thickness in the range of hundreds of micrometers, the superficial impurity layer on the exposed samples seems conveniently removed by physical polishing, chemical etching, and heating in controlled atmosphere. [17–23] However, the energy-density requirment for ASSLBs calls for thin solid electrolyte layers and thick electrodes. In fact, free-standing garnet sheets with thickness below 30 μm have been successfully prepared by suspension-based technologies such as tape casting. [80] For this type of thin sheets, post treatments such as physical polishing or chemical polishing will be either costly or too delicate to operate, which, on the other hand, stresses the necessity to fabricate moisture-stable garnet sheets from the perspective of rationale material design. In addition, this will expand the applications of this material from a solid electrolyte in garnet-based lithium batteries to other fields such as a Li^+-selective membrane for lithium extraction or Li^+-related sensors.

4. Conclusion

Lithium-stuffed garnet, a promising electrolyte material for the all-solid-state lithium batteries, is usually found vulnerable to moisture. Base on the understanding of the reactions between garnets and the moisture, a moisture-stable garnet should possess features including high density, few grain boundaries, controlled secondary phase, and stable grains. This study develops a low-cost, efficient, and solvent-free route based on solid-state reaction to synthesize such garnets. By carefully controlling the stoichiometry of the starting materials and the synthesis route, and subsequently, the morphology, phase formation and relative density of the garnet pellets, a moisture-stable garnet LLZT (Ta5Li0) with no excess Li_2O content is prepared. The as-synthesized Ta5Li0 sample exhibits a morphology of well-connected particles with few grain boundaries, a high room-temperature ionic conductivity of 7.36×10^{-4} S cm^{-1}, and a relative density of 97.5%. The Ta5Li0 also shows outstanding moisture-stability: after the steaming test in an atmosphere rich in H_2O and CO_2 for 24 hours, the ionic conductivity of Ta5Li0 slightly decreases to 6.6×10^{-4} S cm^{-1}; in the water-immersion test, the Ta5Li0 only increases the pH value of the deionized water from 6.0 to 7.7 during the first immersion and barely changes the pH value in the subsequent immersion tests. This moisture-stability of Ta5Li0 can be attributed to, on one hand, the greatly reduced grain boundaries and the substances (e.g., Li_2O) residing at the grain boundaries, and on the other hand, the property of the grains. The absence of the H^+/Li^+ diffusion layer on the Ta5Li0 grains by TOF-SIMS depth-profiling and the reduced reactivity of the Li-deficient garnet lattice with H_2O by DFT calculations suggest the importance of grain property. To further test the lithium compatibility with the garnets, we use the water-immersed Ta5Li0 pellet to assemble symmetric lithium cells and Li|LLZT|LFP cells. The Ta5Li0 pellet exhibits an interfacial resistance of 14.6 Ω cm^2 with Li and enables the Li|LLZT|LFP cell to stably cycle for 100 cycles at 0.5 C and 60°C, which a coulombic efficiency of close to 100% and a discharge capacity of 158.1 mAh g^{-1} at the 100th cycle.

CRediT authorship contribution statement

Hongpeng Zheng: Conceptualization, Methodology, Formal analysis, Data curation, Writing – original draft, Investigation. **Guoyao Li:** Methodology, Investigation, Formal analysis, Data curation, Writing – original draft. **Jiqiong Liu:** Investigation, Software. **Shaoping Wu:** Investigation, Resources. **Xingmin Zhang:** Resources. **Yongmin Wu:** Resources. **Hong Zhu:** Software, Resources. **Xiao Huang:** Conceptualization, Methodology, Formal analysis, Visualization. **Hezhou Liu:** Resources. **Huanan Duan:** Conceptualization, Funding acquisition, Methodology, Formal analysis, Resources, Supervision, Writing – review & editing.

Declaration of Competing Interest

The authors declare that they have no known competing financial interests or personal relationships that could have appeared to influence the work reported in this paper.

Acknowledgments

This work was financially supported by the National Natural Science Foundation of China (no. 51972211) and the Shanghai Aerospace Advanced Technology Joint Research Fund (USCAST2020-32). Instrumental Analysis Center of SJTU and National Engineering Research Center for Nanotechnology are gratefully acknowledged for assisting with relevant experimental analysis. The Center for High-Performance Computing of SJTU is gratefully acknowledged for providing computational facilities for all the simulations.

Supplementary materials

Supplementary material associated with this article can be found, in the online version, at doi:10.1016/j.ensm.2022.04.027.

References

[1] J. Wu, L. Shen, Z. Zhang, G. Liu, Z. Wang, D. Zhou, H. Wan, X. Xu, X. Yao, All-solid-state lithium batteries with sulfide electrolytes and oxide cathodes, Electrochem. Energy Rev. 4 (2021) 101–135, https://doi.org/10.1007/s41918-020-00081-4.
[2] J. Wu, S. Liu, F. Han, X. Yao, C. Wang, Lithium/sulfide all-solid-state batteries using sulfide electrolytes, Adv. Mater. 33 (2021), 2000751, https://doi.org/10.1002/adma.202000751.
[3] S. Chen, D. Xie, G. Liu, J.P. Mwizerwa, Q. Zhang, Y. Zhao, X. Xu, X. Yao, Sulfide solid electrolytes for all-solid-state lithium batteries: structure, conductivity, stability and application, Energy Storage Mater. 14 (2018) 58–74, https://doi.org/10.1016/j.ensm.2018.02.020.
[4] G. Liu, D. Xie, X. Wang, X. Yao, S. Chen, R. Xiao, H. Li, X. Xu, High air-stability and superior lithium ion conduction of $Li_{3+3x}P_{1-x}Zn_xS_{4-x}O_x$ by aliovalent substitution of ZnO for all-solid-state lithium batteries, Energy Storage Mater. 17 (2019) 266–274, https://doi.org/10.1016/j.ensm.2018.07.008.

[5] Y. Zhu, X. He, Y. Mo, Origin of outstanding stability in the lithium solid electrolyte materials: insights from thermodynamic analyses based on first-principles calculations, ACS Appl. Mater. Interfaces 7 (2015) 23685–23693, https://doi.org/10.1021/acsami.5b07517.

[6] J. Wolfenstine, J.L. Allen, J. Read, J. Sakamoto, Chemical stability of cubic Li7La3Zr2O12 with molten lithium at elevated temperature, J. Mater. Sci. 48 (2013) 5846–5851, https://doi.org/10.1007/s10853-013-7380-z.

[7] R. Murugan, V. Thangadurai, W. Weppner, Fast lithium ion conduction in garnet-Type Li7La3Zr2O12, Angew. Chem. Int. Ed. 46 (2007) 7778–7781, https://doi.org/10.1002/anie.200701144.

[8] X. Huang, Y. Lu, Z. Song, K. Rui, Q. Wang, T. Xiu, M.E. Badding, Z. Wen, Manipulating Li2O atmosphere for sintering dense Li7La3Zr2O12 solid electrolyte, Energy Storage Mater. 22 (2019) 207–217, https://doi.org/10.1016/j.ensm.2019.01.018.

[9] Y. Li, B. Xu, H. Xu, H. Duan, X. Lü, S. Xin, W. Zhou, L. Xue, G. Fu, A. Manthiram, J. B. Goodenough, Hybrid polymer/garnet electrolyte with a small interfacial resistance for lithium-ion batteries, Angew. Chem. Int. Ed. 56 (2017) 753–756, https://doi.org/10.1002/anie.201608924.

[10] K. Shi, Z. Wan, L. Yang, Y. Zhang, Y. Huang, S. Su, H. Xia, K. Jiang, L. Shen, Y. Hu, S. Zhang, J. Yu, F. Ren, Y.-B. He, F. Kang, In situ construction of an ultra-stable conductive composite interface for high-voltage all-solid-state lithium metal batteries, Angew. Chem. Int. Ed. 59 (2020) 11784–11788, https://doi.org/10.1002/anie.202000547.

[11] Z. Wan, K. Shi, Y. Huang, L. Yang, Q. Yun, L. Chen, F. Ren, F. Kang, Y.-B. He, Three-dimensional alloy interface between Li6.4La3Zr1.4Ta0.6O12 and Li metal to achieve excellent cycling stability of all-solid-state battery, J. Power Sources 505 (2021), 230062, https://doi.org/10.1016/j.jpowsour.2021.230062.

[12] Y. Tian, F. Ding, H. Zhong, C. Liu, Y.-B. He, J. Liu, X. Liu, Q. Xu, Li6.75La3Zr1.75Ta0.25O12@amorphous Li3OCl composite electrolyte for solid state lithium-metal batteries, Energy Storage Mater. 14 (2018) 49–57, https://doi.org/10.1016/j.ensm.2018.02.015.

[13] W. Xia, B. Xu, H. Duan, X. Tang, Y. Guo, H. Kang, H. Li, H. Liu, Reaction mechanisms of lithium garnet pellets in ambient air: the effect of humidity and CO2, J. Am. Ceram. Soc. 100 (2017) 2832–2839, https://doi.org/10.1111/jace.14865.

[14] R.H. Brugge, A.K.O. Hekselman, A. Cavallaro, F.M. Pesci, R.J. Chater, J.A. Kilner, A. Aguadero, Garnet electrolytes for solid state batteries: visualization of moisture-induced chemical degradation and revealing its impact on the Li-ion dynamics, Chem. Mater. 30 (2018) 3704–3713, https://doi.org/10.1021/acs.chemmater.8b00486.

[15] W. Xia, B. Xu, H. Duan, Y. Guo, H. Kang, H. Li, H. Liu, Ionic conductivity and air stability of Al-doped Li7La3Zr2O12 sintered in alumina and Pt crucibles, ACS Appl. Mater. Interfaces 8 (2016) 5335–5342, https://doi.org/10.1021/acsami.5b12186.

[16] L. Cheng, C.H. Wu, A. Jarry, W. Chen, Y. Ye, J. Zhu, R. Kostecki, K. Persson, J. Guo, M. Salmeron, G. Chen, M. Doeff, Interrelationships among grain size, surface composition, air stability, and interfacial resistance of Al-substituted Li7La3Zr2O12 solid electrolytes, ACS Appl. Mater. Interfaces 7 (2015) 17649–17655, https://doi.org/10.1021/acsami.5b02528.

[17] C. Wang, H. Xie, W. Ping, J. Dai, G. Feng, Y. Yao, S. He, J. Weaver, H. Wang, K. Gaskell, L. Hu, A general, highly efficient, high temperature thermal pulse toward high performance solid state electrolyte, Energy Storage Mater. 17 (2019) 234–241, https://doi.org/10.1016/j.ensm.2018.11.007.

[18] H. Huo, X. Li, Y. Sun, X. Lin, K. Doyle-Davis, J. Liang, X. Gao, R. Li, H. Huang, X. Guo, X. Sun, Li2CO3 effects: new insights into polymer/garnet electrolytes for dendrite-free solid lithium batteries, Nano Energy 73 (2020), 104836, https://doi.org/10.1016/j.nanoen.2020.104836.

[19] J.-F. Wu, B.-W. Pu, D. Wang, S.-Q. Shi, N. Zhao, X. Guo, X. Guo, In situ formed shields enabling Li2CO3-free solid electrolytes: a new route to uncover the intrinsic lithiophilicity of garnet electrolytes for dendrite-free Li-metal batteries, ACS Appl. Mater. Interfaces 11 (2019) 898–905, https://doi.org/10.1021/acsami.8b18356.

[20] A. Sharafi, E. Kazyak, A.L. Davis, S. Yu, T. Thompson, D.J. Siegel, N.P. Dasgupta, J. Sakamoto, Surface chemistry mechanism of ultra-low interfacial resistance in the solid-state electrolyte Li7La3Zr2O12, Chem. Mater. 29 (2017) 7961–7968, https://doi.org/10.1021/acs.chemmater.7b03002.

[21] H. Huo, Y. Chen, N. Zhao, X. Lin, J. Luo, X. Yang, Y. Liu, X. Guo, X. Sun, In-situ formed Li2CO3-free garnet/Li interface by rapid acid treatment for dendrite-free solid-state batteries, Nano Energy 61 (2019) 119–125, https://doi.org/10.1016/j.nanoen.2019.04.058.

[22] M. Motoyama, Y. Tanaka, T. Yamamoto, N. Tsuchimine, S. Kobayashi, Y. Iriyama, The active interface of Ta-doped Li7La3Zr2O12 for Li plating/stripping revealed by acid aqueous etching, ACS Appl. Energy Mater. 2 (2019) 6720–6731, https://doi.org/10.1021/acsaem.9b01193.

[23] B. Wu, S. Wang, J. Lochala, D. Desrochers, B. Liu, W. Zhang, J. Yang, J. Xiao, The role of the solid electrolyte interphase layer in preventing Li dendrite growth in solid-state batteries, Energy Environ. Sci. 11 (2018) 1803–1810, https://doi.org/10.1039/C8EE00540K.

[24] X. Zeng, A.J. Martinolich, K.A. See, K.T. Faber, Dense garnet-type electrolyte with coarse grains for improved air stability and ionic conductivity, J. Storage Mater. 27 (2020), 101128, https://doi.org/10.1016/j.est.2019.101128.

[25] Y. Li, Y. Cao, X. Guo, Influence of lithium oxide additives on densification and ionic conductivity of garnet-type Li6.75La3Zr1.75Ta0.25O12 solid electrolytes, Solid State Ionics 253 (2013) 76–80, https://doi.org/10.1016/j.ssi.2013.09.005.

[26] Y. Jin, P.J. McGinn, Li7La3Zr2O12 electrolyte stability in air and fabrication of a Li/Li7La3Zr2O12/Cu0.1V2O5 solid-state battery, J. Power Sources 239 (2013) 326–331, https://doi.org/10.1016/j.jpowsour.2013.03.155.

[27] Y. Ren, Y. Shen, Y. Lin, C.-W. Nan, Direct observation of lithium dendrites inside garnet-type lithium-ion solid electrolyte, Electrochem. Commun. 57 (2015) 27–30, https://doi.org/10.1016/j.elecom.2015.05.001.

[28] Y. Suzuki, K. Kami, K. Watanabe, A. Watanabe, N. Saito, T. Ohnishi, K. Takada, R. Sudo, N. Imanishi, Transparent cubic garnet-type solid electrolyte of Al2O3-doped Li7La3Zr2O12, Solid State Ionics 278 (2015) 172–176, https://doi.org/10.1016/j.ssi.2015.06.009.

[29] X. Huang, T. Xiu, M.E. Badding, Z. Wen, Two-step sintering strategy to prepare dense Li-garnet electrolyte ceramics with high Li+ conductivity, Ceram. Int. 44 (2018) 5660–5667, https://doi.org/10.1016/j.ceramint.2017.12.217.

[30] L. Cheng, J.S. Park, H. Hou, V. Zorba, G. Chen, T. Richardson, J. Cabana, R. Russo, M. Doeff, Effect of microstructure and surface impurity segregation on the electrical and electrochemical properties of dense Al-substituted Li7La3Zr2O12, J. Mater. Chem. A 2 (2014) 172–181, https://doi.org/10.1039/C3TA13999A.

[31] S.G. Kang, D.S. Sholl, First-principles study of chemical stability of the lithium oxide garnets Li7La3M2O12 (M = Zr, Sn, or Hf), J. Phys. Chem. C 118 (2014) 17402–17406, https://doi.org/10.1021/jp504314w.

[32] R. Kun, F. Langer, M. Delle Piane, S. Ohno, W.G. Zeier, M. Gockeln, L. Colombi Ciacchi, M. Busse, I. Fekete, Structural and computational assessment of the influence of wet-chemical post-processing of the Al-substituted cubic Li7La3Zr2O12, ACS Appl. Mater. Interfaces 10 (2018) 37188–37197, https://doi.org/10.1021/acsami.8b09789.

[33] K. Liu, J.-T. Ma, C.-A. Wang, Excess lithium salt functions more than compensating for lithium loss when synthesizing Li6.5La3Ta0.5Zr1.5O12 in alumina crucible, J. Power Sources 260 (2014) 109–114, https://doi.org/10.1016/j.jpowsour.2014.02.065.

[34] E.A. Dobretsov, Y.G. Mateyshina, N.F. Uvarov, Influence of lithium oxide excess and alumina on grain boundary resistance of Li6.75La3Zr1.75Nb0.25O12 solid electrolyte, Solid State Ionics 299 (2017) 55–59, https://doi.org/10.1016/j.ssi.2016.09.014.

[35] H. Zheng, S. Wu, R. Tian, Z. Xu, H. Zhu, H. Duan, H. Liu, Intrinsic lithiophilicity of Li–garnet electrolytes enabling high-rate lithium cycling, Adv. Funct. Mater. 30 (2020), 1906189, https://doi.org/10.1002/adfm.201906189.

[36] W. Kohn, L.J. Sham, Self-consistent equations including exchange and correlation effects, Phys. Rev. 140 (1965) A1133–A1138, https://doi.org/10.1103/PhysRev.140.A1133.

[37] S.L. Dudarev, G.A. Botton, S.Y. Savrasov, C.J. Humphreys, A.P. Sutton, Electron-energy-loss spectra and the structural stability of nickel oxide: an LSDA+U study, Phys. Rev. B 57 (1998) 1505–1509, https://doi.org/10.1103/PhysRevB.57.1505.

[38] H.J. Monkhorst, J.D. Pack, Special points for Brillouin-zone integrations, Phys. Rev. B 13 (1976) 5188–5192, https://doi.org/10.1103/PhysRevB.13.5188.

[39] Recommended reference materials for realization of physicochemical properties, Pure Appl. Chem. 52 (1980) 2393–2404, https://doi.org/10.1351/pac198052102393.

[40] M.W.J. Chase, C.A. Davies, J.R.J. Downey, D.J. Frurip, R.A. McDonald, A. N. Syverud, JANAF thermochemical tables: third edition. II: Cr-Zr, J. Phys. Chem. Ref. Data 14 (1985) 927–1856.

[41] V. Thangadurai, W. Weppner, Li6ALa2Ta2O12 (A = Sr, Ba): novel garnet-like oxides for fast lithium ion conduction, Adv. Funct. Mater. 15 (2005) 107–112, https://doi.org/10.1002/adfm.200400044.

[42] B. Xu, H. Duan, W. Xia, Y. Guo, H. Kang, H. Li, H. Liu, Multistep sintering to synthesize fast lithium garnets, J. Power Sources 302 (2016) 291–297, https://doi.org/10.1016/j.jpowsour.2015.10.084.

[43] Y. Ji, C. Zhou, F. Lin, B. Li, F. Yang, H. Zhu, J. Duan, Z. Chen, Submicron-sized Nb-doped lithium garnet for high ionic conductivity solid electrolyte and performance of quasi-solid-state lithium battery, Materials 13 (2020), https://doi.org/10.3390/ma13030560.

[44] X. Huang, Y. Lu, H. Guo, Z. Song, T. Xiu, M.E. Badding, Z. Wen, None-mother-powder method to prepare dense Li-garnet solid electrolytes with high critical current density, ACS Appl. Energy Mater. 1 (2018) 5355–5365, https://doi.org/10.1021/acsaem.8b00976.

[45] M. Kotobuki, K. Kanamura, Y. Sato, T. Yoshida, Fabrication of all-solid-state lithium battery with lithium metal anode using Al2O3-added Li7La3Zr2O12 solid electrolyte, J. Power Sources 196 (2011) 7750–7754, https://doi.org/10.1016/j.jpowsour.2011.04.047.

[46] J. Gai, E. Zhao, F. Ma, D. Sun, X. Ma, Y. Jin, Q. Wu, Y. Cui, Improving the Li-ion conductivity and air stability of cubic Li7La3Zr2O12 by the co-doping of Nb, Y on the Zr site, J. Eur. Ceram. Soc. 38 (2018) 1673–1678, https://doi.org/10.1016/j.jeurceramsoc.2017.12.002.

[47] H. Buschmann, S. Berendts, B. Mogwitz, J. Janek, Lithium metal electrode kinetics and ionic conductivity of the solid lithium ion conductors “Li7La3Zr2O12” and Li7−xLa3Zr2−xTaxO12 with garnet-type structure, J. Power Sources 206 (2012) 236–244, https://doi.org/10.1016/j.jpowsour.2012.01.094.

[48] X. Huang, C. Shen, K. Rui, J. Jin, M. Wu, X. Wu, Z. Wen, Influence of La2Zr2O7 additive on densification and Li+ conductivity for Ta-doped Li7La3Zr2O12 garnet, JOM 68 (2016) 2593–2600, https://doi.org/10.1007/s11837-016-2065-0.

[49] P. Pourghahramani, E. Altin, M.R. Mallembakam, W. Peukert, E. Forssberg, Microstructural characterization of hematite during wet and dry millings using Rietveld and XRD line profile analyses, Powder Technol. 186 (2008) 9–21, https://doi.org/10.1016/j.powtec.2007.10.027.

[50] A.L. Ortiz, F. Sánchez-Bajo, V.M. Candelario, F. Guiberteau, Comminution of B4C powders with a high-energy mill operated in air in dry or wet conditions and its effect on their spark-plasma sinterability, J. Eur. Ceram. Soc. 37 (2017) 3873–3884, https://doi.org/10.1016/j.jeurceramsoc.2017.05.034.

[51] Y. Wang, W. Lai, Phase transition in lithium garnet oxide ionic conductors Li7La3Zr2O12: the role of Ta substitution and H2O/CO2 exposure, J. Power Sources 275 (2015) 612–620, https://doi.org/10.1016/j.jpowsour.2014.11.062.
[52] I.N. David, T. Thompson, J. Wolfenstine, J.L. Allen, J. Sakamoto, Microstructure and Li-ion conductivity of hot-pressed cubic Li7La3Zr2O12, J. Am. Ceram. Soc. 98 (2015) 1209–1214, https://doi.org/10.1111/jace.13455.
[53] S. Qin, X. Zhu, Y. Jiang, M.e. Ling, Z. Hu, J. Zhu, Extremely dense microstructure and enhanced ionic conductivity in hot-isostatic pressing treated cubic garnet-type solid electrolyte of Ga2O3-doped Li7La3Zr2O12, Funct. Mater. Lett. 11 (2018), 1850029, https://doi.org/10.1142/S1793604718500297.
[54] S.-W. Baek, J.-M. Lee, T.Y. Kim, M.-S. Song, Y. Park, Garnet related lithium ion conductor processed by spark plasma sintering for all solid state batteries, J. Power Sources 249 (2014) 197–206, https://doi.org/10.1016/j.jpowsour.2013.10.089.
[55] C.-Y. Huang, Y.-T. Tseng, H.-Y. Lo, J.-K. Chang, W.-W. Wu, In situ atomic scale investigation of Li7La3Zr2O12-based Li+-conducting solid electrolyte during calcination growth, Nano Energy 71 (2020), 104625, https://doi.org/10.1016/j.nanoen.2020.104625.
[56] R.P. Rao, W. Gu, N. Sharma, V.K. Peterson, M. Avdeev, S. Adams, In situ neutron diffraction monitoring of Li7La3Zr2O12 formation: toward a rational synthesis of garnet solid electrolytes, Chem. Mater. 27 (2015) 2903–2910, https://doi.org/10.1021/acs.chemmater.5b00149.
[57] P.J. Kumar, K. Nishimura, M. Senna, A. Düvel, P. Heitjans, T. Kawaguchi, N. Sakamoto, N. Wakiya, H. Suzuki, A novel low-temperature solid-state route for nanostructured cubic garnet Li7La3Zr2O12 and its application to Li-ion battery, RSC Adv. 6 (2016) 62656–62667, https://doi.org/10.1039/C6RA09695F.
[58] J.K. Padarti, T.T. Jupalli, C. Hirayama, M. Senna, T. Kawaguchi, N. Sakamoto, N. Wakiya, H. Suzuki, Low-temperature processing of garnet-type ion conductive cubic Li7La3Zr2O12 powders for high performance all solid-type Li-ion batteries, J. Taiwan Inst. Chem. Eng. 90 (2018) 85–91, https://doi.org/10.1016/j.jtice.2018.02.021.
[59] M. Matsui, K. Sakamoto, K. Takahashi, A. Hirano, Y. Takeda, O. Yamamoto, N. Imanishi, Phase transformation of the garnet structured lithium ion conductor: Li7La3Zr2O12, Solid State Ionics 262 (2014) 155–159, https://doi.org/10.1016/j.ssi.2013.09.027.
[60] A. Paolella, W. Zhu, G. Bertoni, S. Savoie, Z. Feng, H. Demers, V. Gariepy, G. Girard, E. Rivard, N. Delaporte, A. Guerfi, H. Lorrmann, C. George, K. Zaghib, Discovering the influence of lithium loss on garnet Li7La3Zr2O12 electrolyte phase stability, ACS Appl. Energy Mater. 3 (2020) 3415–3424, https://doi.org/10.1021/acsaem.9b02401.
[61] Y. Li, Z. Wang, C. Li, Y. Cao, X. Guo, Densification and ionic-conduction improvement of lithium garnet solid electrolytes by flowing oxygen sintering, J. Power Sources 248 (2014) 642–646, https://doi.org/10.1016/j.jpowsour.2013.09.140.
[62] S. Ohta, J. Seki, Y. Yagi, Y. Kihira, T. Tani, T. Asaoka, Co-sinterable lithium garnet-type oxide electrolyte with cathode for all-solid-state lithium ion battery, J. Power Sources 265 (2014) 40–44, https://doi.org/10.1016/j.jpowsour.2014.04.065.
[63] W. Lu, T. Wang, M. Xue, C. Zhang, Improved Li6.5La3Zr1.5Nb0.5O12 electrolyte and effects of atmosphere exposure on conductivities, J. Power Sources 497 (2021), 229845, https://doi.org/10.1016/j.jpowsour.2021.229845.
[64] A. Orera, G. Larraz, J.A. Rodríguez-Velamazán, J. Campo, M.L. Sanjuán, Influence of Li+ and H+ distribution on the crystal structure of Li7–xHxLa3Zr2O12 ($0 \leq x \leq 5$) garnets, Inorg. Chem. 55 (2016) 1324–1332, https://doi.org/10.1021/acs.inorgchem.5b02708.
[65] C. Liu, K. Rui, C. Shen, M.E. Badding, G. Zhang, Z. Wen, Reversible ion exchange and structural stability of garnet-type Nb-doped Li7La3Zr2O12 in water for applications in lithium batteries, J. Power Sources 282 (2015) 286–293, https://doi.org/10.1016/j.jpowsour.2015.02.050.
[66] T.H. Wan, M. Saccoccio, C. Chen, F. Ciucci, Influence of the discretization methods on the distribution of relaxation times deconvolution: implementing radial basis functions with DRTtools, Electrochim. Acta 184 (2015) 483–499, https://doi.org/10.1016/j.electacta.2015.09.097.
[67] A. Weiß, S. Schindler, S. Galbiati, M.A. Danzer, R. Zeis, Distribution of relaxation times analysis of high-temperature PEM fuel cell impedance spectra, Electrochim. Acta 230 (2017) 391–398, https://doi.org/10.1016/j.electacta.2017.02.011.
[68] B.A. Boukamp, Derivation of a distribution function of relaxation times for the (fractal) finite length Warburg, Electrochim. Acta 252 (2017) 154–163, https://doi.org/10.1016/j.electacta.2017.08.154.
[69] M. Hahn, D. Rosenbach, A. Krimalowski, T. Nazarenus, R. Moos, M. Thelakkat, M. A. Danzer, Investigating solid polymer and ceramic electrolytes for lithium-ion batteries by means of an extended Distribution of Relaxation Times analysis, Electrochim. Acta 344 (2020), 136060, https://doi.org/10.1016/j.electacta.2020.136060.
[70] L. Zhuang, X. Huang, Y. Lu, J. Tang, Y. Zhou, X. Ao, Y. Yang, B. Tian, Phase transformation and grain-boundary segregation in Al-Doped Li7La3Zr2O12 ceramics, Ceram. Int. 47 (2021) 22768–22775, https://doi.org/10.1016/j.ceramint.2021.04.295.
[71] J. Meng, Y. Zhang, X. Zhou, M. Lei, C. Li, Li2CO3-affiliative mechanism for air-accessible interface engineering of garnet electrolyte via facile liquid metal painting, Nat. Commun. 11 (2020) 3716, https://doi.org/10.1038/s41467-020-17493-x.
[72] Y. Lu, X. Huang, Y. Ruan, Q. Wang, R. Kun, J. Yang, Z. Wen, An in situ element permeation constructed high endurance Li–LLZO interface at high current densities, J. Mater. Chem. A 6 (2018) 18853–18858, https://doi.org/10.1039/C8TA07241H.
[73] S.A. Pervez, G. Kim, B.P. Vinayan, M.A. Cambaz, M. Kuenzel, M. Hekmatfar, M. Fichtner, S. Passerini, Overcoming the interfacial limitations imposed by the solid–solid interface in solid-state batteries using ionic liquid-based interlayers, Small 16 (2020), 2000279, https://doi.org/10.1002/smll.202000279.
[74] M. Wu, D. Liu, D. Qu, Z. Xie, J. Li, J. Lei, H. Tang, 3D coral-like LLZO/PVDF composite electrolytes with enhanced ionic conductivity and mechanical flexibility for solid-state lithium batteries, ACS Appl. Mater. Interfaces 12 (2020) 52652–52659, https://doi.org/10.1021/acsami.0c15004.
[75] Z. Sun, Y. Lai, N. Lv, L. Jiang, M. Jia, J. Li, W. Bao, F. Liu, Transition metal dichalcogenides in alliance with Ag ameliorate the interfacial connection between Li anode and garnet solid electrolyte, J. Power Sources 468 (2020), 228379, https://doi.org/10.1016/j.jpowsour.2020.228379.
[76] Y. Li, J.-T. Han, C.-A. Wang, H. Xie, J.B. Goodenough, Optimizing Li+ conductivity in a garnet framework, J. Mater. Chem. 22 (2012) 15357–15361, https://doi.org/10.1039/C2JM31413D.
[77] C.R. Mariappan, K.I. Gnanasekar, V. Jayaraman, T. Gnanasekaran, Lithium ion conduction in Li5La3Ta2O12 and Li7La3Ta2O13 garnet-type materials, J. Electroceram. 30 (2013) 258–265, https://doi.org/10.1007/s10832-013-9792-1.
[78] M.W.J. Chase, NIST-JANAF themochemical tables, fourth edition, J. Phys. Chem. Ref. Data Monograph 9 (1998) 1–1951.
[79] R. Jalem, Y. Yamamoto, H. Shiiba, M. Nakayama, H. Munakata, T. Kasuga, K. Kanamura, Concerted migration mechanism in the Li ion dynamics of garnet-type Li7La3Zr2O12, Chem. Mater. 25 (2013) 425–430, https://doi.org/10.1021/cm303542x.
[80] G.T. Hitz, D.W. McOwen, L. Zhang, Z. Ma, Z. Fu, Y. Wen, Y. Gong, J. Dai, T. R. Hamann, L. Hu, E.D. Wachsman, High-rate lithium cycling in a scalable trilayer Li-garnet-electrolyte architecture, Mater. Today 22 (2019) 50–57, https://doi.org/10.1016/j.mattod.2018.04.004.